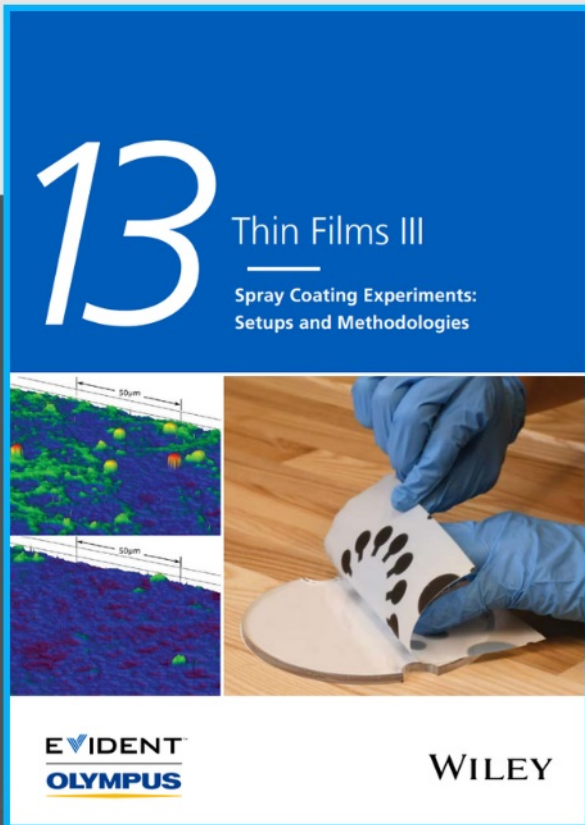




Spray Coating Experiments: Setups and Methodologies



**The latest eBook from
Advanced Optical Metrology.
Download for free.**

Spray Coating Experiments: Setups and Methodologies, is the third in our Thin Films eBook series. This publication provides an introduction to spray coating, three article digests from Wiley Online Library and the latest news about Evident's Image of the Year Award 2022.

Wiley in collaboration with Evident, are committed to bridging the gap between fundamental research and industrial applications in the field of optical metrology. We strive to do this by collecting and organizing existing information, making it more accessible and useful for researchers and practitioners alike.

EVIDENT
OLYMPUS

WILEY

Lanthanide Contraction Builds Better High-Voltage LiCoO₂ Batteries

Jing Xia, Na Zhang, Yijun Yang, Xing Chen, Xi Wang,* Feng Pan,* and Jiannian Yao*

Cycling lithium cobalt oxide (LiCoO₂) to a potential higher than 4.35 V (vs Li⁺/Li) can obtain an enticing capacity, but suffers from inferior structural stability. Herein, an ingenious Li-deintercalation/doping strategy is developed to synthesize the lanthanide-doped LiCoO₂ (lanthanide (Ln) = praseodymium, neodymium, samarium, europium, gadolinium, erbium, or lutetium) with Ln occupying Li-sites. Electrochemical measurements show that the cycling stability of Ln-doped LiCoO₂ increases as the lanthanide contracts. By rule, lutetium-doped LiCoO₂ exhibits the best cycling stability, confirmed in both lithium half-cell and pouch full-cell. Comprehensive experimental characterizations combining with theoretical calculations reveal that the lattice strain tuned by the lanthanide contraction plays a critical role in the structure stability of LiCoO₂. This finding is an important step for building better high-voltage LiCoO₂ batteries, as it is possible to achieve better high-voltage performance by combining the doping technology and performance improvement rule disclosed in this study.

1. Introduction

Lithium-ion batteries (LIBs), a popular energy storage device with high energy/power density, have been widely used in portable electronics, and recently in electric vehicles.^[1] However, with the progress in science and technology, the energy density of existing LIBs is difficult to keep up with the ever-increasing demand for battery endurance. Electrode materials, especially cathode materials, are the key for obtaining high energy density because they have a direct bearing on the working voltage and capacity of batteries.

Lithium cobalt oxide (LiCoO₂), the preferred cathode material for portable electronic products, can further tap its unexploited capacity and energy density by increasing the upper cut-off voltage.^[2] However, the inferior structural stability

of LiCoO₂ at potentials higher than 4.35 V (vs Li⁺/Li) leads to unsatisfactory cycle life.^[3] Many researchers have intensively studied the high-voltage LiCoO₂ (≥4.5 V) and improved its cycle life by various modification strategies, especially foreign ion doping.^[1b,c,2c,4] For example, Ren's group^[1b] reported that the La-Al co-doping could improve the structural stability of LiCoO₂ at 4.5 V by suppressing the phase transitions during cycling. Both Li's group^[1c] and Cu's group^[4d] synthesized Al-Ti-Mg co-doped LiCoO₂ and achieved stable cycling at 4.6 V by the synergistic regulation of the three elements. In addition to transition metal ion doping, non-metallic doping such as F and Se is also proven to be effective in improving the high voltage stability of LiCoO₂.^[4e,5] These foreign ions have a certain difference in ion radius. Therefore, some scientific questions are worth pondering: Are the doping of foreign ions with inappropriate sizes affect the high-voltage stability of LiCoO₂? How is it affected? And how much impact on it? These questions, if answered well, could provide a reference for the selection of foreign ions to develop better high-voltage LiCoO₂ batteries and improve the structural stability of other layered cathode materials. Thus, it is first and foremost to select some elements with similar chemical properties but different ionic radii for doping of LiCoO₂, and all elements must be doped at the same site, namely Li site, Co site, or O site.

Lanthanide elements (denoted as Ln) have similar chemical properties because they have a same outer electronic configuration except for the number of 4f electrons.^[6] As the atomic number increases, electrons are added gradually to the poorly shielding 4f orbitals resulting in an increase in effective nuclear

J. Xia
College of Chemistry and Chemical Engineering
Xiamen University
Xiamen 361005, P. R. China

J. Xia
Innovation Laboratory for Sciences and Technologies of Energy Materials
of Fujian Province (IKKEM)
Xiamen 361102, P. R. China

N. Zhang, X. Chen
Institute of Molecular Plus
Tianjin University
Tianjin 300072, P. R. China

Y. Yang, X. Wang
Department of Physics, School of Physical Science and Engineering
Beijing Jiaotong University
Beijing 100044, P. R. China
E-mail: xiwang@bjtu.edu.cn

F. Pan
School of Advanced Materials
Peking University
Shenzhen Graduate School
Shenzhen 518055, P. R. China
E-mail: panfeng@pku.edu.cn

J. Yao
Beijing National Laboratory for Molecular Sciences
Institute of Chemistry
Chinese Academy of Science
Beijing 100190, P. R. China
E-mail: jnyao@iccas.ac.cn

 The ORCID identification number(s) for the author(s) of this article can be found under <https://doi.org/10.1002/adfm.202212869>.

DOI: 10.1002/adfm.202212869

charge and, correspondingly, a decrease in ionic radii, which is the so-called lanthanide contraction.^{16,71} Inspired by this, we developed an ingenious Li-deintercalation/doping strategy to fabricate the Ln-doped LiCoO₂ (Ln-LCOs, Ln = Pr, Nd, Sm, Eu, Gd, Er, Lu) with Ln cations occupying Li-sites, and surprisingly found that their cycling stability increased as the lanthanide contraction. The experimental results unequivocally linked the ionic radius of the Ln cations to the high-voltage stability of Ln-LCOs, where the ionic radius modulates the high-voltage stability of Ln-LCOs by changing the lattice strain. Combined with the theoretical analysis, we demonstrated how the lanthanide contraction improved the electrochemical performance of Ln-LCOs.

2. Synthesis and Characterizations

In order to achieve targeted doping at the Li sites, a new Li-deintercalation/doping strategy is proposed to prepare Ln-LCOs (Figure 1a). The synthesis details of the samples are presented in the Methods section. Simply put, the commercial LiCoO₂ with bulk morphology was first fabricated into working electrodes and electrochemically delithiated in Li half-cells to form Li_{1-x}□_xCoO₂. A small amount of Li-deintercalation leads to an increase in the electrostatic repulsion between adjacent Co—O slabs, thus increases the layer spacing of LiCoO₂ (Figure S1, Supporting Information), which is conducive to the incorporation

of large-sized Ln cations. The as-prepared Li_{1-x}□_xCoO₂ was thoroughly mixed with Ln(NO₃)₃·xH₂O (Ln = Pr, Nd, Sm, Eu, Gd, Er, and Lu) and absolute ethyl alcohol by ball-milling, and then calcined at high temperature to obtain Li_{1-x}Ln_xCoO₂. X-ray photoelectron spectroscopy (XPS, Figure S2, Supporting Information) results show that the Co peaks of Ln-LCOs are shifted to a lower binding energy than PLCO, indicating that the charge balance in Ln-LCOs is maintained by reducing the valence of Co. The morphology of LiCoO₂ barely changed after ball milling except that more LiCoO₂ particles were exposed on the surface of the electrode (Figure S3, Supporting Information). Besides, all the prepared LiCoO₂ showed similar morphology (Figure S4, Supporting Information), indicating that lanthanide doping has a negligible effect on the morphology of LiCoO₂.

The X-ray diffraction (XRD) patterns in Figure 1b demonstrated the successful preparation of various Ln-LCOs. The (003)/(104) peak intensity ratio of all Ln-LCOs was reduced significantly compared with pristine LiCoO₂ (denoted as PLCO), suggesting that Ln cations were doped in their lithium layers. Rietveld refinements (Figure S5, Supporting Information) also further confirmed the occupation of Ln cations in 3a sites. To further verify the doping site of the Ln cations, using Lu-LCO as a prototype, we compared the structural differences between PLCO and Lu-LCO at the atomic level by scanning transmission electron microscopy with high angle annular dark field detection (STEM-HAADF). As shown in Figures 1c,d, both PLCO and Lu-LCO exhibit well-ordered layered structure. Compared

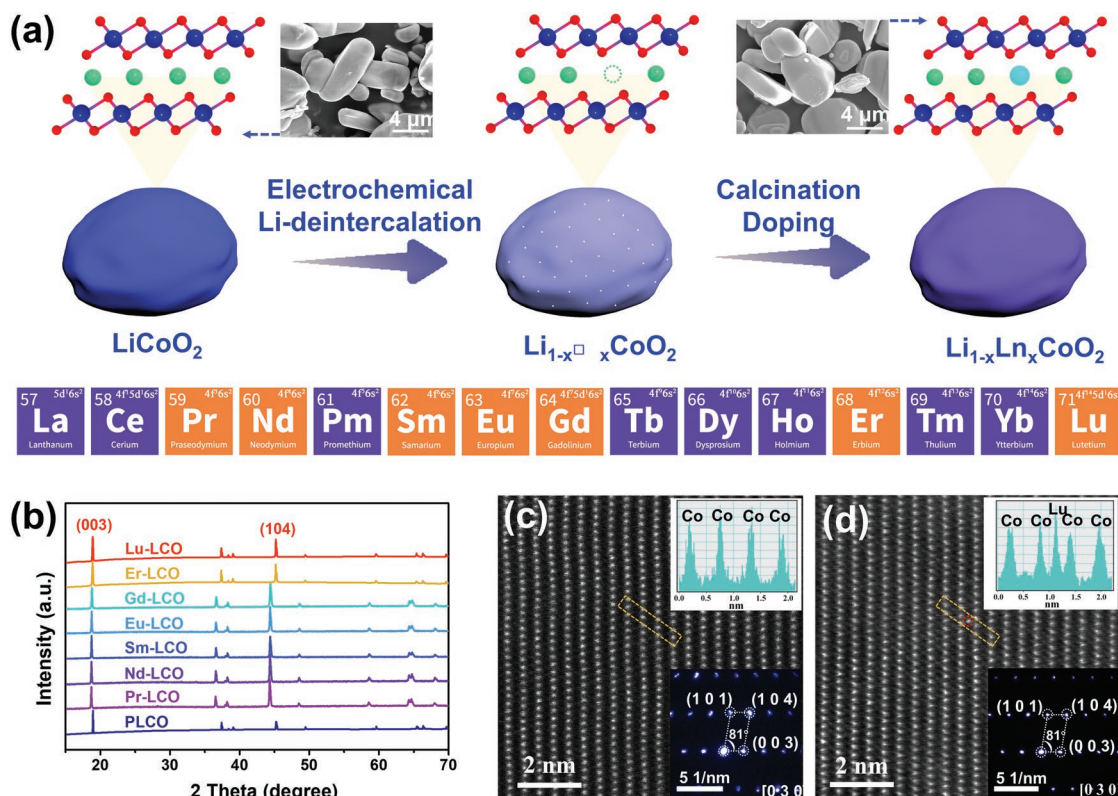


Figure 1. a) Schematic diagram of targeted doping of Ln cations in LiCoO₂. b) XRD patterns of PLCO and various Ln-LCOs. c,d) Atomic resolution STEM-HAADF images of PLCO and Lu-LCO, and their corresponding intensity plot (top right inset) and nano beam diffraction pattern (bottom right inset). O atoms and Li atoms cannot be observed in the HAADF mode due to their low atomic mass, but strong signals (marked with red dotted circles) can be observed in the Li layers of Lu-LCO, suggesting that the Lu atoms are doped in the Li layers.

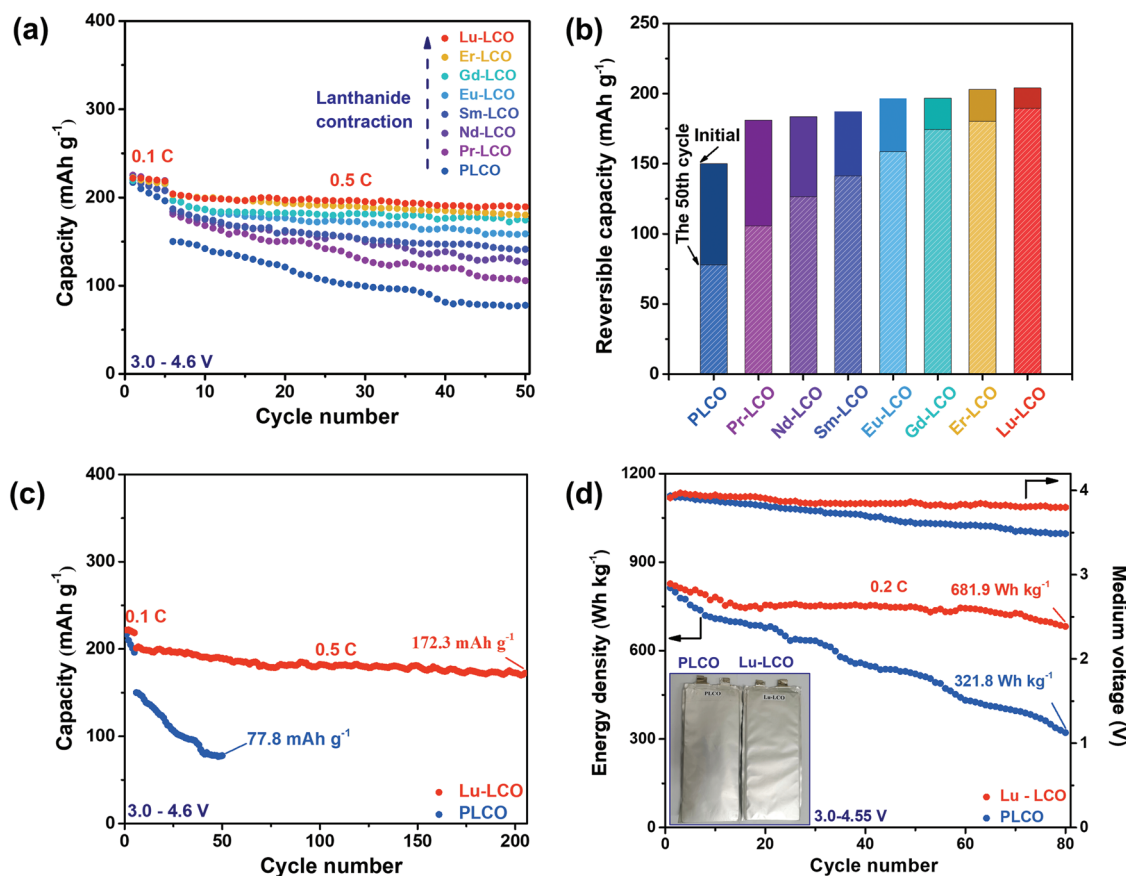


Figure 2. a) Cycling performance of PLCO and various Ln-LCOs in half-cell in the potential range of 3.0–4.6 V. b) The initial and 50th cycle discharge capacity of PLCO and various Ln-LCOs. c) Cycling performance of PLCO and Lu-LCO in a half-cell in the potential range of 3.0–4.6 V. d) Energy density of the cathode materials (PLCO or Lu-LCO) and medium voltage of the pouch cells as a function of cycle number. The LiCoO₂/graphite pouch-cells were cycled at 0.2 C in the voltage window of 3.0–4.55 V (equivalent to 4.6 V versus Li⁺/Li). Inset: pouch cells after 80 cycles. For PLCO-graphite pouch cell, obvious gas generation can be observed, indicating a large amount of oxygen release.

to PLCO, the strong signals can be observed in the Li layers of Lu-LCO (Figure 1d), suggesting that the Lu atoms occupy the 3a sites of Li atoms, which further proves that Ln cations are incorporated into the Li layers. The electrochemically inert Ln cations can act as the pillars to support the Co–O slabs, and thus preventing their structural collapse at the high delithiation state.

3. Electrochemical Performance

The electrochemical performance of PLCO and as-prepared Ln-LCOs was evaluated in Li half-cells using metal Li as the counter/reference electrode. As shown in Figure 2a, the eight samples deliver similar initial capacity of ≈220 mAh g⁻¹ at 0.1 C in the potential range of 3.0–4.6 V, but all Ln-LCOs show enhanced cycling stability compared with PLCO. Figure 2b reports the reversible capacities before and after cycling test at 0.5 C for all the Ln-LCOs and PLCO. The cycling stability of these eight samples is ranked as follows: PLCO < Pr-LCO < Nd-LCO < Sm-LCO < Eu-LCO < Gd-LCO < Er-LCO < Lu-LCO, that is, the cycling stability of the seven Ln-LCOs follows the same direction as lanthanide contraction, indicating that

lanthanide contraction leads to the improvement of cycling stability. By rule, it is expected that Lu-LCO will exhibit a longer cycle life. As shown in Figure 2c, further cycling tests indicate that Lu-LCO indeed shows a long cycle life with a high capacity of 172.3 mAh g⁻¹ at 0.5 C after 200 cycles. Not only that, Lu-LCO delivered a high capacity of 147.4 mAh g⁻¹ even at a rate of 2 C (Figure S6b, Supporting Information).^[1b,c,4a,c,e,8] For potential battery applications, Lu-LCO exhibited a stable energy density/medium voltage of 681.9 Wh kg⁻¹ (≈179.4 mAh g⁻¹, Figure S7, Supporting Information)/3.80 V in a pouch full-cell after 80 cycles (Figure 2d), demonstrating its availability in commercial high-voltage LiCoO₂ batteries.

To reveal the modulation mechanism of Lu doping on the high-voltage stability of LiCoO₂, various characterization techniques, including in situ XRD, STEM-HAADF, XPS, and synchrotron X-ray absorption spectroscopy (sXAS) were conducted. The detailed discussion was provided in the Supplementary Text of Supporting Information (Figures S8–S19 and Table S2, Supporting Information). To sum up, the Lu atoms in the Li layers

can act as pillars to support the Co–O slabs and thus reducing the lattice strain of the LiCoO_2 by reducing the variation of the interlayer spacing. Because of such structure advantages, the detrimental phase transitions, oxygen release, microcrack formation, and electrolyte decomposition were suppressed. It has been reported that the lanthanide elements all have very similar chemical properties,^[9] Bader charge analysis was conducted to compare the effects of Ln cations in Ln-LCOs (Figure S20, Supporting Information). As expected, the charges around all Ln atoms have negligible differences, but are far more negative than those around Li atoms, indicating that the Ln cations can introduce additional electrons for the O atoms to reduce the charge compensation of lattice oxygen, and thus improving the stability of lattice oxygen. Therefore, gas evolution in Lu-LCO-graphite pouch cells was significantly suppressed compared to PLCO-graphite pouch cells (inset of Figure 2d). Due to the similar chemical properties of the lanthanide elements, the above-proposed modulation mechanism for the high-voltage stability of Lu-LCO is also applicable for other Ln-LCOs. Hence, the relationship between lanthanide contraction and structural stability of LiCoO_2 will be discussed below.

4. Relationship between Lanthanide Contraction and Structural Stability of LiCoO_2

Although the modulation mechanism of lanthanide elements on the high voltage stability of LiCoO_2 has been revealed by the detailed analysis using Lu-LCO as a prototype, the reasons why

the electrochemical performance of Ln-LCOs change regularly with lanthanide contraction remains unexplained. To understand how lanthanide contraction affects the electrochemical performance of Ln-LCOs, the synthesized samples were firstly studied by XPS and XRD techniques. XPS identified that Ln ions in Ln-LCOs have a valence state of +3 (Figure S21, Supporting Information), so their ionic radii conform to the law of lanthanide contraction. From Pr-LCO to Lu-LCO, the (003) diffraction peak gradually shifts to higher 2θ angles (Figure 3a), illustrating that the c-axis spacing of Ln-LCOs decreases with the decrease of Ln ion radius. The lattice parameters simulated by theoretical calculations also have the same rules as above (Figure S22, Supporting Information). Furthermore, Rietveld refined lattice parameter *c* has a linear correlation with the length of calculated Ln–O bonds, as shown in Figure 3b. Based on these interesting experiment phenomena, it can be preliminarily concluded that the gradual improvement of the high-voltage stability of Ln-LCOs with lanthanide contraction is related to their crystal structure.

In fact, XRD experiment results are the overall average of the tested samples. We suspect that the doping of foreign ions will only cause changes in its local structure rather than all regions. Therefore, we compared the spacing between two adjacent Co atoms at different positions by theoretical simulation. As shown in Figure 3c and Table S3 (Supporting Information), the spacing between the two Co layers closest to the Ln atom is greatly enlarged, while the spacing between the next closest Co layers is smaller than the former. Interestingly, in the region far away from Ln atom, the Co–Co spacing is almost

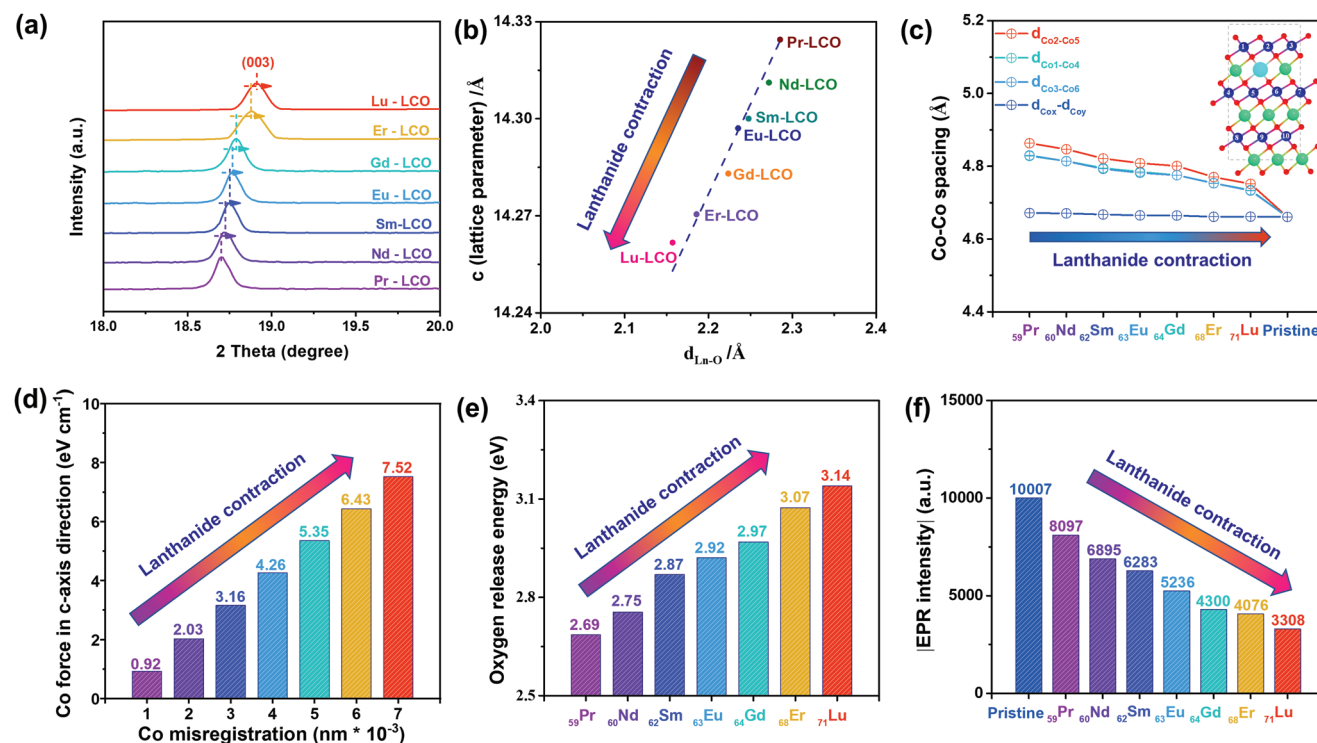


Figure 3. a) XRD patterns of various Ln-LCOs at the (003) diffraction peak. b) Relationship between the Rietveld refined lattice parameter *c* of Ln-LCOs and the bond length of the Ln–O bonds. The dotted line shows the linear fit. c) Co–Co spacing of PLCO and Ln-LCOs along the c-axis. Co_{*x*} and Co_{*y*} are located far away from Ln atom. d) Co force along the c-axis direction in the LiCoO_2 structure, as a function of different degrees of Co misregistration. e) Oxygen release energy of the oxygen atom closest to the Ln ion in Ln-LCOs. f) EPR intensity variation tendency of the after-cycled PLCO and Ln-LCOs.

unchanged. Therefore, it can be deduced that the doping of Ln cations with excessively large size will cause large Co misregistration or lattice strain. Furthermore, the theoretical calculations on the structural stability of Ln-LCOs, expressed as Co force and oxygen release energy,^[10] elucidate that the stability increases as the lattice strain decreases, i.e., lattice strain is a stability descriptor. Specifically, the Co force gradually decreases (Figure 3d and Table S4, Supporting Information) and the oxygen release energy gradually increases (Figure 3e) with the lanthanide elements from left to right, indicating that the stability of Co and lattice oxygen was improved gradually.

Based on the above analysis, we further conducted the post-mortem studies on the cycled electrodes through XRD and electron paramagnetic resonance (EPR) experiments. From the XRD patterns in Figure S23a (Supporting Information), all diffraction peaks of Lu-LCO electrode can be indexed to the hexagonal LiCoO_2 with R-3m space group, and the well-split (006)/(102) peaks indicate that the layered structure was well maintained. In contrast, the diffraction peaks of other Ln-LCOs gradually weaken or even disappear in the opposite direction of the lanthanide contraction, especially PLCO, most of its diffraction peaks disappeared and the (003) peak was obviously split (Figure S23b, Supporting Information), indicating that a new spinel phase was generated in after-cycled PLCO, and its crystal structure was severely damaged.^[11] This damage must be accompanied by the loss of lattice oxygen, thus the EPR experiments were conducted to study the generation of oxygen vacancies in the LiCoO_2 (Figure S24, Supporting Information). Figure 3f shows the EPR intensity variation tendency

of the after-cycled PLCO and Ln-LCOs. The decrease in EPR signal intensity with lanthanide contraction implies a gradual decrease in oxygen release, which is consistent with the above experimental results. Therefore, the reduction of lattice strain caused by lanthanide contraction also affects the structural stability of LiCoO_2 for long-term cycling.

5. In Situ Experiments and Improvement Mechanism

To further reveal the effects of Ln cations on the electrochemical performance and structural stability of LCO, in situ XRD was performed to study the structural evolution of PLCO and Ln-LCOs during the first charge and discharge. As shown in Figure 4a, all samples underwent similar phase transitions during charging. However, when the cells were discharged to 3.0 V, a new peak, representing the H3 phase,^[4a] appeared in PLCO (Figure 4a1) and Pr-LCO (Figure 4a2), implying that they have a low structural reversibility. Moreover, the variation range of the (003) peak of Ln-LCOs gradually decreases with lanthanide contraction (Figure 4a). The variation range of the (003) peak can be quantified as the variation of layer spacing according to Bragg's Law, as shown in Figure 4b. Obviously, the variation in layer spacing of Ln-LCOs decreasing in the same direction as lanthanide contraction, which is beneficial to reducing the lattice strain of Ln-LCOs along the c-axis direction and thus enhancing the electrochemical reversibility of Ln-LCOs. This deduction was further confirmed by the

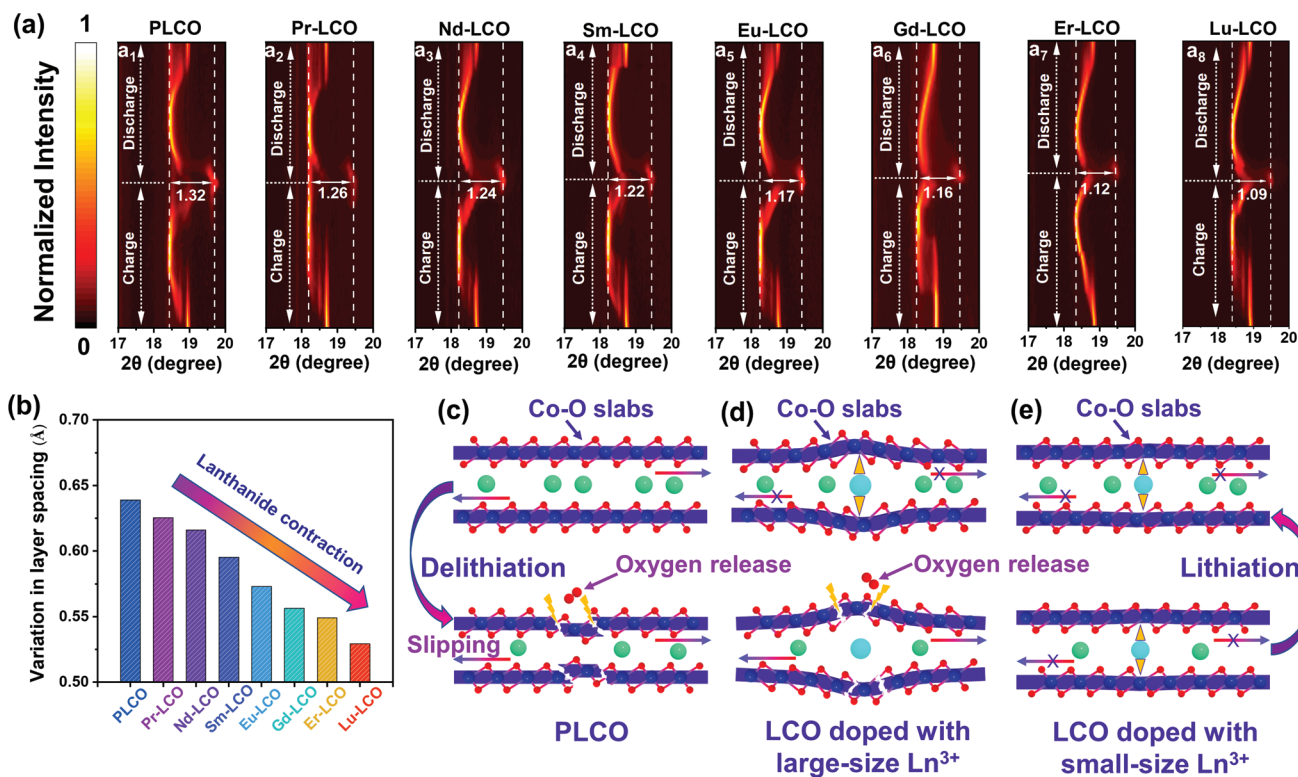


Figure 4. a) In situ XRD evolution of PLCO and Ln-LCOs at the (003) diffraction peak. b) The change values in layer spacing of PLCO and Ln-LCOs. c-e) Structural evolution mechanism of PLCO, LCO doped with large-sized Ln^{3+} , and LCO doped with small-sized Ln^{3+} .

cyclic voltammetry (CV, Figure S25, Supporting Information) experiments.

Overall, the lattice parameters, Co force, oxygen release energy, and (003) peak variation range of Ln-LCOs all are linearly correlated with the Ln cation radius. Here a modulation mechanism of lanthanide contraction on the high voltage stability of LiCoO_2 was proposed, as shown in Figure 4c–e. At low voltages, the extraction of Li ions from PLCO leads to an increase in the electrostatic repulsion between adjacent Co–O slabs, causing their slippage in the a- and/or b-axis directions and thus detrimental phase transitions (Top half of Figure 4c). It has been reported that the Ln–O bond is stronger than the Li–O bond,^[12] so the Ln cations can suppress the slippage of the Co–O slabs and thus low-voltage phase transitions of Ln-LCOs (Top half of Figure 4d,e). When the cells were charged to a higher voltage, PLCO showed inferior structural stability (Bottom half of Figure 4c), such as adverse Co–O slab slipping, structural collapse, irreversible phase transitions, and gaseous oxygen release, due to the lack of structural support for Co–O slabs.^[13] But the electrochemically inert Ln cations in the Li layer can act as a pillar to support the Co–O slabs and thus alleviating the structural deterioration of Ln-LCOs. These are the reasons why the electrochemical performance of all Ln-LCOs was improved compared to PLCO. Since the inherent large lattice strain, Ln-LCOs doped with large-size lanthanide ions, typically Pr-LCO, cannot tolerate the structure deterioration caused by the extraction of a large number of Li ions (Bottom half of Figure 4d). Therefore, even though the high voltage stability of Pr-LCO was significantly improved compared to PLCO, it showed the worst electrochemical performance among all Ln-LCOs. As the ionic radii decreases across the lanthanide series, the structural stability and electrochemical performance of Ln-LCOs are enhanced by reducing the lattice strain through the lanthanide contraction. Because of Lu^{3+} has the closest ionic radius to Li^+ , Lu doping is more favorable to improve the structural stability of LiCoO_2 (Bottom half of Figure 4e), thus Lu-LCO shows the best electrochemical performance among all Ln-LCOs.

6. Conclusion

In summary, we selected seven lanthanide elements with similar chemical properties for doping of LiCoO_2 , and demonstrated how the ionic radius affect the electrochemical performance of Ln-LCOs. Electrochemical measurements indicate that all Ln-LCOs show enhanced cycling stability compared with PLCO, and the cycling stability of the seven Ln-LCOs enhancing in the same direction as lanthanide contraction. Using various characterization techniques and theoretical calculations, we concluded that the lattice strain is a descriptor for the structural stability of LiCoO_2 , while the ionic radius is the initiator of lattice strain changes. To be specific, the electrochemically inert Ln cations in the Li layer can act as anchored pillars to suppress the irreversible phase transitions and enhance the stability of lattice oxygen. However, the large-sized Ln cation doping induces an increase in the lattice strain of Ln-LCOs, so Ln-LCOs doped with large-size Ln cations, typically Pr-LCO, cannot endure the structure deterioration caused by the extraction of a large

number of Li ions. In the direction of lanthanide contraction, the radius of the Ln cations gradually decreases, so the electrochemical performance of Ln-LCOs gradually improves with lanthanide contraction, especially Lu-LCO, which exhibits the best electrochemical performance among all Ln-LCOs. Therefore, we firmly believe that the careful structural design, for instance, by using this rule to wisely select foreign ions, in combination with multiple modification strategies, could yield record-breaking LiCoO_2 battery performance in practical applications.

7. Experimental Section

Material Synthesis: Battery grade LiCoO_2 (Canrd, China), and analytically pure grade $\text{Ln}(\text{NO}_3)_3 \cdot x\text{H}_2\text{O}$ (Aladdin, China) were used as raw materials to prepare Ln-LCOs (Ln = Pr, Nd, Sm, Eu, Gd, Er, and Lu). For the synthesis of various Ln-LCOs, commercial LiCoO_2 (wt. 80%), polyvinylidene fluoride (PVDF) binder (wt. 10%), and carbon black (wt. 10%) were first mixed, and fabricated into a thin sheet by the powder tablet method. The thin sheet was used as a working electrode to match with lithium metal sheet and assemble into pouch Li half-cell, then the Li half-cell was charged to achieve the Li-deintercalation. The amount of lithium ions removed was controlled at ≈ 1 mole% by limiting the charging capacity. After electrochemical delithiation, the cell was disassembled to obtain electrochemically delithiated LiCoO_2 ($\text{Li}_{1-x}\square_x\text{CoO}_2$). The after-tested electrode was rinsed with dimethyl carbonate (DMC) to remove the electrolyte residue on the electrode surface, and then dried at 80°C . Finally, the $\text{Li}_{1-x}\square_x\text{CoO}_2$ was thoroughly mixed with $\text{Ln}(\text{NO}_3)_3 \cdot x\text{H}_2\text{O}$ and an appropriate amount of absolute ethyl alcohol by ball-milling, and subsequently calcined in air at 1000°C for 10 h to form Ln-LCOs. The excess of 5 wt.% $\text{Ln}(\text{NO}_3)_3 \cdot x\text{H}_2\text{O}$ was added to compensate for the Ln loss during high-temperature synthesis. During the calcination process, PVDF binder and carbon black were removed due to thermal decomposition, and Ln cations were doped in the LiCoO_2 structure. In the synthesis process, LiCoO_2 maintains its hexagonal structure without change in all synthesis stages (Figure S1a, Supporting Information). After electrochemical delithiation, the (003) diffraction peak of LiCoO_2 shifted slightly to a lower 2θ angle (Figure S1b, Supporting Information), indicating that the interlayer spacing of LiCoO_2 was enlarged, which is conducive to the incorporation of large-sized Ln cations. After calcination doping, the (003) peak shifted to a lower 2θ angle, which proved that the Ln cations were successfully doped in the lithium layer. In this work, we optimized the Lu doping content of Lu-LCO, and the results indicated that Lu-LCO doped with 1% Lu has the best electrochemical performance (Figure S6, Supporting Information). Therefore, the performance comparison between various Ln-LCOs was also based on 1% Ln doping.

X-Ray Diffraction (XRD): The X-ray diffraction (XRD) measurements were conducted on a SmartLab (Rigaku, 9kW) diffractometer with $\text{Cu K}\alpha$ X-ray source ($\lambda = 1.5406 \text{ \AA}$) at a scan rate of 5 min^{-1} between 15 to 70° (2θ). To obtain the lattice parameters of samples, the XRD patterns were fitted using Rietveld method by the general structure analysis software (GSAS), and the $w\text{Rp}$ and Rp values of all samples were controlled $<5\%$ to ensure the reliability of the fitting results. A specially designed cell device equipped with beryllium (Be) window was used to conduct the in situ XRD experiments. The in situ XRD patterns were recorded within the 2θ range of 15 – 25° during charging/discharging at a current density of 0.2 C ($1\text{C} = 274 \text{ mA g}^{-1}$), and the interval time for each 2θ scan was 4 min.

Micromorphology and Microstructure Observation: The micromorphology of samples was observed by a FEI Apreo S LoVac field-emission scanning electron microscope (FE-SEM). The atomic resolution STEM-HAADF (scanning transmission electron microscopy with high angle annular dark field detection) imaging, nano-beam diffraction (NBD), and spatially resolved EDS were characterized by a Titan G2 60–300 microscope (300 kW) equipped with a probe spherical

aberration corrector and “super X” EDS system. Since the electron beam cannot penetrate micron-sized particles, the particles were thinned to <200 nm by a FEI Helios DualBeam Focused Ion Beam (FIB) operated at 2–30 kV. To prevent the specimen from being damaged and contaminated by the Ga ion beam, 1.5 μm thick Pt layer was deposited on the surface of the particles before lift-out and thinning.

X-Ray Photoelectron Spectroscopy (XPS): The surface chemistry of samples was investigated by ESCALAB 250 XI X-ray photoelectron spectroscopy (Thermo Scientific) with a Mg/Al Kα x-ray source. The binding energy of all samples was calibrated by C1s peak at 284.6 eV as the internal standard.

Electron Paramagnetic Resonance (EPR): Electron paramagnetic resonance (EPR) spectrometer is an extremely powerful tool for detecting oxygen vacancies and oxygen free radicals. The evolution of lattice oxygen of samples was investigated using Bruker A300-10/12 electron paramagnetic resonance spectrometer with a magnetic field of 100 kHz. For the preparation of EPR samples, PLCO/Li and Ln-LCOs/Li half-cells were disassembled after cycled at 0.1 C for the first 5 cycles and 0.5 C for subsequent 45 cycles, and the after-cycled electrodes were rinsed with dimethyl carbonate (DMC) to remove the electrolyte residue on the electrode surface. The symmetrical EPR signal peaks centered at $g \approx 2.003 \pm 0.001$ represent the O⁻ free radicals or oxygen vacancies.^[14] In addition, all EPR tests were performed at a low temperature of 100 K.

Synchrotron X-Ray Spectroscopy: All synchrotron X-ray spectroscopy (XAS) studies were performed at the Beijing Synchrotron Radiation Facility (BSRF, China). Soft X-ray absorption spectroscopy (sXAS) measurements at the O K-edge were conducted at beamline 4B7B. Hard X-ray spectroscopy (hXAS) measurements at the Co K-edge were performed at beamline 1W1B. Note that the pristine samples and after-cycled samples were performed in the transmission mode and fluorescence mode, respectively. The hXAS data were analyzed by the Demeter software package. Quantitative curve fitting of the k³-weighted extended X-ray absorption fine structure (EXAFS) oscillation was performed within 0–4 Å using the ARTEMIS module of IFEFFIT. In this work, the cells for XRD, EPR, TEM, and XAS characterizations were tested in Li half-cells at 0.1 C for the first 5 cycles and 0.5 C for subsequent 45 cycles. Before the characterization of after-cycled electrodes, which were rinsed with dimethyl carbonate (DMC) to remove the electrolyte residue on the electrode surface.

Fabrication of Half-Cells: The electrochemical properties of LiCoO₂/Li half-cells were conducted using CR2032 coin cells. For the fabrication of working electrodes, active materials (wt. 80%), polyvinylidene fluoride (PVDF) binder (wt. 10%), and carbon black (wt. 10%) were first mixed in N-Methyl pyrrolidone (NMP) solvent to form a homogeneous slurry. The obtained slurry was coated on an aluminum metal current collector, and then dried at 80 °C for 12 h. The loading of cathode active materials in all half-cells was controlled within the range of 3–4 mg cm⁻². The coin cells were assembled in an argon-filled glovebox using lithium metal as counter electrode, Celgard 2025 membrane as separator, and the solution composed of 1 M LiPF₆ in ethylene carbonate/dimethyl carbonate/ethyl methyl carbonate (EC : DMC : EMC = 1 : 1 : 1 vol.%) as electrolyte.

Fabrication of Pouch Full-Cells: For the fabrication of pouch full-cells, the cathode electrodes were prepared by mixing the cathode materials (wt. 95%), super-P (wt. 3%), and PVDF (wt. 2%) in NMP to form a homogeneous slurry, and coating the slurry to both sides of the aluminum metal current collector, followed by drying at 80 °C for 12 h. The areal density of cathode materials was controlled within the range of 6–7 mg cm⁻¹ (both sides of the current collector were 12–14 mg cm⁻¹). The anode electrodes were prepared by mixing the commercial graphite (wt. 95%), super-P (wt. 2%), carboxy methyl cellulose sodium (CMC, wt. 1.5%), styrene butadiene rubber (SBR, wt. 1.5%) in deionized water to form a homogeneous slurry, and coating the slurry on a copper metal current collector, followed by drying at 80 °C for 12 h. The areal density of anode materials was adjusted according to the capacity ratio of 1.05–1.10 between anode and cathode. The separator and electrolyte used in the pouch full-cells were the same as those used in the half-cells.

Electrochemical Measurements: The electrochemical measurements of half-cells were conducted on a Land CT2001A battery test system.

The electrochemical properties of all cells were measured at room temperature. For the half-cell tests, galvanostatic charge/discharge mode was performed. For the pouch full-cell tests, an additional constant voltage mode was added during the charging process. For the long-term cycle test, the pouch full-cells were first charged to 4.55 V at a constant current of 0.2 C, and then charged at a constant voltage of 4.55 V until the current dropped to 0.01 C.

Note that the fresh pouch full-cells were cycled at low current densities for the pre-formation process before the long-term cycle test. Specifically, the pouch full-cells were charged at a constant current of 0.01 C for 2 h followed by resting for 10 min, and then charged to 4.55 V at a constant current of 0.01 C and charged at a constant voltage of 4.55 V until the current dropped to 0.01 C. After resting for 4 h at room temperature, the pouch full-cells were discharged to 3 V at a constant current of 0.01 C. Finally, the pouch full-cells were rested at 50 °C for 48 h to promote the contact between electrodes and electrolyte.

First Principles Calculations: The spin-polarized density functional theory (DFT) calculations were performed via the projected augmented wave (PAW) method^[15] implemented in Vienna Ab initio Simulation Package (VASP)^[16] with the Perdew–Burke–Ernzerhof (PBE) exchange-correlation functional of generalized gradient approximation.^[17] The lanthanides-doped LiCoO₂ were modeled by substituting one out of 27 Li or Co ions in the 3 × 3 super cell. The plane-wave cutoff energy was set at 500 eV. For geometry optimization, the lattice parameters and all atoms were free to move in all directions until the force on each atom was <=0.02 eV Å⁻¹ and the energy convergence threshold was set to 10⁻⁵ eV. The Brillouin zone was sampled with 3 × 3 × 2 Gamma-centered k-point grid. The oxygen release energy of Ln-LCOs in the full Li state was calculated by removing the oxygen atom closest to the doped lanthanide atom. The calculation formula was as follows: $\Delta E = E_{O_2} + E_{Li_{1-x}Co_xO_2} - E_{LiCoO_2}$, where the E_{O₂} represents the energy of oxygen molecule, the E_{Li_{1-x}Co_xO₂} denotes the energy of defect LiCoO₂ with one oxygen vacancy, and the E_{LiCoO₂} stands for the total energy of perfect lanthanides-doped LiCoO₂. For the calculation of Co force, all atoms and cell parameters were relaxed except the fixed c coordinates of the Co atoms. The misalignment values of Co in the c-axis were set as 0, 0.01, 0.02, 0.03, 0.04, 0.05, 0.06, and 0.07 Å, respectively.

Supporting Information

Supporting Information is available from the Wiley Online Library or from the author.

Acknowledgements

This work was supported financially by the “Key Program for International S&T Cooperation Projects of China” from the Ministry of Science and Technology of China (grant no. 2018YFE0124600), and National Natural Science Foundation of China (grant nos. 91961125 and 21905019), and Chemistry and Chemical Engineering Guangdong Laboratory (no. 1932004), and Science and Technology Project of Guangdong Province (no. 2020B0101370001), and the Project from China Petrochemical Corporation (no. S20L00151).

Conflict of Interest

The authors declare no conflict of interest.

Author Contributions

J.X. and N.Z. contributed equally to this work. J.X. contributed in conceptualization, data curation, formal analysis, investigation,

methodology, and writing-original draft. N.Z. contributed in data curation, and investigation. X.C. and Y.Y. contributed in methodology. X.W. contributed in conceptualization, funding administration, resources, supervision, validation, writing-review and editing. F.P. and J.Y. contributed in resources, validation, writing-review and editing.

Data Availability Statement

The data that support the findings of this study are available in the supplementary material of this article.

Keywords

cathode materials, dopants, high-voltage LiCoO₂, lanthanide contraction, lithium-ion batteries

Received: November 5, 2022

Revised: November 20, 2022

Published online: December 11, 2022

- [1]) F. Lin, D. Nordlund, Y. Li, M. K. Quan, L. Cheng, T.-C. Weng, Y. Liu, H. L. Xin, M. M. Doeff, *Nat. Energy* **2016**, *1*, 15004; b) Q. Liu, X. Su, D. Lei, Y. Qin, J. Wen, F. Guo, Y. A. Wu, Y. Rong, R. Kou, X. Xiao, F. Aguesse, J. Bareño, Y. Ren, W. Lu, Y. Li, *Nat. Energy* **2018**, *3*, 936; c) J.-N. Zhang, Q. Li, C. Ouyang, X. Yu, M. Ge, X. Huang, E. Hu, C. Ma, S. Li, R. Xiao, W. Yang, Y. Chu, Y. Liu, H. Yu, X.-Q. Yang, X. Huang, L. Chen, H. Li, *Nat. Energy* **2019**, *4*, 594; d) W. Lee, S. Muhammad, C. Sergey, H. Lee, J. Yoon, Y.-M. Kang, W.-S. Yoon, *Angew. Chem., Int. Ed.* **2020**, *59*, 2578.
- [2] a) K. Mizushima, P. C. Jones, P. J. Wiseman, J. B. Goodenough, *Mater. Res. Bull.* **1980**, *15*, 783; b) Y. Lyu, X. Wu, K. Wang, Z. Feng, T. Cheng, Y. Liu, M. Wang, R. Chen, L. Xu, J. Zhou, Y. Lu, B. Guo, *Adv. Energy Mater.* **2020**, *11*, 2000982; c) S. Kalluri, M. Yoon, M. Jo, S. Park, S. Myeong, J. Kim, S. X. Dou, Z. Guo, J. Cho, *Adv. Energy Mater.* **2017**, *7*, 1601507.
- [3] a) A. Van der Ven, M. K. Aydinol, G. Ceder, G. Kresse, J. Hafner, *Phys. Rev. B* **1998**, *58*, 2975; b) G. G. Amatucci, J. M. Tarascon, L. C. Klein, *J. Electrochem. Soc.* **1996**, *143*, 1114.
- [4] a) Y. Huang, Y. Zhu, H. Fu, M. Ou, C. Hu, S. Yu, Z. Hu, C. T. Chen, G. Jiang, H. Gu, H. Lin, W. Luo, Y. Huang, *Angew. Chem., Int. Ed.* **2021**, *60*, 4682; b) J. Qian, L. Liu, J. Yang, S. Li, X. Wang, H. L. Zhuang, Y. Lu, *Nat. Commun.* **2018**, *9*, 4918; c) R. Gu, Z. Ma, T. Cheng, Y. Lyu, A. Nie, B. Guo, *ACS Appl. Mater. Interfaces* **2018**, *10*, 31271; d) L. Wang, J. Ma, C. Wang, X. Yu, R. Liu, F. Jiang, X. Sun, A. Du, X. Zhou, G. Cui, *Adv. Sci.* **2019**, *6*, 1900355; e) Z. Zhu, H. Wang, Y. Li, R. Gao, X. Xiao, Q. Yu, C. Wang, I. Waluyo, J. Ding, A. Hunt, J. Li, *Adv. Mater.* **2020**, *32*, 2005182; f) S. Song, Y. Li, K. Yang, Z. Chen, J. Liu, R. Qi, Z. Li, C. Zuo, W. Zhao, N. Yang, *J. Mater. Chem. A* **2021**, *9*, 5702.
- [5] a) W. Kong, J. Zhang, D. Wong, W. Yang, J. Yang, C. Schulz, X. Liu, *Angew. Chem., Int. Ed.* **2021**, *60*, 27102; b) W. Huang, Q. Zhao, M. Zhang, S. Xu, H. Xue, C. Zhu, J. Fang, W. Zhao, G. Ren, R. Qin, Q. Zhao, H. Chen, F. Pan, *Adv. Energy Mater.* **2022**, *12*, 2200813.
- [6] I. D. Hughes, M. Däne, A. Ernst, W. Hergert, M. Lüders, J. Poulter, J. B. Staunton, A. Svane, Z. Szotek, W. M. Temmerman, *Nature* **2007**, *446*, 650.
- [7] a) M. Seitz, A. G. Oliver, K. N. Raymond, *J. Am. Chem. Soc.* **2007**, *129*, 11153; b) J. H. Lee, R. H. Byrne, *Geochim. Cosmochim. Acta* **1992**, *56*, 1127.
- [8] a) J. Qian, L. Liu, J. Yang, S. Li, X. Wang, H. L. Zhuang, Y. Lu, *Nat. Commun.* **2018**, *9*, 4918; b) Q. Yang, J. Huang, Y. Li, Y. Wang, J. Qiu, J. Zhang, H. Yu, X. Yu, H. Li, L. Chen, *J. Power Sources* **2018**, *388*, 65.
- [9] D. A. Johnson, *J. Chem. Educ.* **1980**, *57*, 475.
- [10] J. Li, C. Lin, M. Weng, Y. Qiu, P. Chen, K. Yang, W. Huang, Y. Hong, J. Li, M. Zhang, C. Dong, W. Zhao, Z. Xu, X. Wang, K. Xu, J. Sun, F. Pan, *Nat. Nanotechnol.* **2021**, *16*, 599.
- [11] G. Zhang, X. Pan, K. Yu, M. Yan, F. Xiong, L. Wu, X. Deng, H. Zhang, L. Mai, *Chem. Res. Chin. Univ.* **2020**, *36*, 690.
- [12] a) J. K. Gibson, *J. Phys. Chem. A* **2003**, *107*, 7891; b) X. Chen, Y. K. Bai, C. Z. Zhao, X. Shen, Q. Zhang, *Angew. Chem., Int. Ed.* **2020**, *59*, 11192.
- [13] a) M. Yoon, Y. Dong, Y. Yoo, S. Myeong, J. Hwang, J. Kim, S. H. Choi, J. Sung, S. J. Kang, J. Li, J. Cho, *Adv. Funct. Mater.* **2019**, *30*, 1907903; b) Y. Jiang, C. Qin, P. Yan, M. Sui, *J. Mater. Chem. A* **2019**, *7*, 20824; c) W. Cho, S. Myeong, N. Kim, S. Lee, Y. Kim, M. Kim, S. J. Kang, N. Park, P. Oh, J. Cho, *Adv. Mater.* **2017**, *29*, 1605578.
- [14] V. A. Shvets, V. B. Sapozhnikov, N. D. Chuvylkin, V. B. Kazansky, *J. Catal.* **1978**, *52*, 459.
- [15] G. Kresse, D. Joubert, *Phys. Rev. B* **1999**, *59*, 1758.
- [16] G. Kresse, J. Furthmüller, *Phys. Rev. B* **1996**, *54*, 11169.
- [17] a) J. P. Perdew, K. Burke, M. Ernzerhof, *Phys. Rev. Lett.* **1996**, *77*, 3865; b) J. P. Perdew, M. Ernzerhof, K. Burke, *J. Chem. Phys.* **1996**, *105*, 9982.